Journal of Power Sources 667 (2026) 239261

Contents lists available at ScienceDirect

Journal of Power Sources

journal homepage: www.elsevier.com/locate/jpowsour

Impact of electrolyte and SEI passivity on thermal runaway: A comparative DSC and ARC analysis of anode-free lithium metal batteries

Dongliang Chen [a,1], Jie Liao [b,1], Zachary J. Trdinich [b], Chaoyang Wang [c,*], Feifei Shi [a,b,**]

[a] John and Willie Leone Family Department of Energy and Mineral Engineering, The Pennsylvania State University, University Park, PA, 16802, United States
[b] Department of Materials Science and Engineering, The Pennsylvania State University, University Park, PA, 16802, United States
[c] Department of Mechanical Engineering, The Pennsylvania State University, University Park, PA, 16802, United States

HIGHLIGHTS

- Combined ARC and DSC to link small-scale Li-electrolyte reactions with full-cell thermal runaway in NCM811/Cu AFLMBs.
- Thermal runaway of AFLMBs is more severe at higher SOC, higher C-rate, and after cycling.
- LHCE forms a dense, LiF-rich SEI that postpones exotherms and lowers the max heating rate compared with LP40.

ABSTRACT

During battery safety tests, there is a typical discrepancy between small-scale coin cells and large-format pouch cells. Academic studies usually employ small-scale coin cells using differential scanning calorimetry (DSC) for fundamental understanding, whereas industry relies on large-scale cells using accelerating rate calorimetry (ARC) to evaluate safety risks, leading to a critical knowledge gap in translating lab-scale findings to practical applications. In this work, we assessed the safety of anode free lithium metal batteries (AFLMBs) for both large and small scales by comparing DSC and ARC. The higher state of charge (SOC) and cycling numbers will reduce AFLMB safety, and higher charge rates tend to form a more reactive lithium metal anode. The passivation effect of solid electrolyte interphase (SEI) on deposited lithium can reduce the self-heating temperature rate of the battery after cycling. This work bridges the understanding of AFLMBs' safety from small scale to large scales, which will greatly benefit the knowledge translation between academia and industry.

1. Introduction

Anode free lithium metal batteries (AFLMBs) are promising candidates for the next-generation lithium-based batteries due to their higher energy density and low manufacturing costs [1,2]. However, their commercialization is hindered by short cycle life and safety concerns related to thermal runaway that are exacerbated by dendrite growth, electrolyte instability, and thermal incompatibility between components [3,4]. Before developing battery safety related electrode/electrolyte modification and interface engineering strategies, a rational and standardized approach to evaluate the battery safety and quantify the thermal runaway is a prerequisite for improving thermodynamic safety performance for AFLMBs. In many thermal performance tests, the thermal runaway measurement of batteries is simulated by destructive and extreme condition tests [5–7]. Although the simulation of battery failure has approached the actual application scenarios, the battery state condition used for battery safety tests lacks a reliable and consistent benchmark. Besides, there are gaps between the understanding and testing of battery safety on an industrial scale and that on a laboratory scale. These gaps are derived from (1) differences in cell formats (pouch or cylindrical cells for industry, coin cells for laboratory), and (2) differences in measurement methods, for examples, nail penetration (NP) or accelerating rate calorimetry (ARC) for industry and differential scanning calorimetry (DSC) for laboratory [8–10]. As a result, different thermal runaway evaluation methods are often applied to different types of cells. However, there is a certain preference for the reliability of data obtained when using the same method to test different battery stages. Therefore, for a more comprehensive assessment of battery safety, a detailed thermal analysis protocol is also required in addition to the benchmark of the state conditions of the battery to be

---

* Corresponding author.

** Corresponding author. John and Willie Leone Family Department of Energy and Mineral Engineering, The Pennsylvania State University, University Park, PA, 16802, United States.

E-mail addresses: cxw31@psu.edu (C. Wang), feifeishi@psu.edu (F. Shi).

[1] These authors contributed equally to this work.

https://doi.org/10.1016/j.jpowsour.2026.239261
Received 20 October 2025; Received in revised form 17 December 2025; Accepted 4 January 2026

tested.

Current safety evaluation methods regarding thermal runaway include NP (commonly used for cylindrical cells and pouch cells) [11,12], ARC (for pouch cells) [3,13], and DSC (for laboratory-scale battery components) [14,15]. The NP based on abuse tests exhibits poor repeatability, as microscopic structural inconsistencies may lead to different rates of thermal propagation at different probing positions. Furthermore, such penetration often induces different types of internal short circuits and makes it difficult to pinpoint the initiation site of thermal runaway, thus limiting its reliability for systematic studies [5,11,16]. ARC and DSC have emerged as two promising thermodynamic assessment techniques to evaluate not only the heat generation and exothermic reactions in lithium batteries but also the thermal compatibility between battery components [15,17,18]. However, these two methods are limited by the battery cell format. ARC is the industry standard for cell-level safety, integrating all coupled thermal and gas evolution processes. Thus, it is hard to identify the specific contributions of individual battery components, especially in pouch cells, for which the burst of thermal runaway is a collection of enthalpy changes of many micro-short circuits [19,20]. DSC excels in laboratory mechanistic studies, providing a more accessible approach to evaluate the reaction enthalpy and phase transitions of small size battery components. It is conducted under controlled, small-scale, and typically inert conditions, but real-world hazards (runaway onset, peak temperature) as measured by ARC are typically understated by DSC alone [21,22]. Therefore, the knowledge gap between these two techniques lies in the interaction between the heat release of micro-short circuit and total thermal runaway of the integral device and correlation of evaluation indicators, which makes the understanding and quantification of thermal runaway remain stagnant.

In this work, we first compare the working principle, temperature indicators, and pros and cons of three common thermal analysis methods (NP, ARC, and DSC). Thermal stability between the cycled lithium metal anode and electrolyte is assessed with DSC, while the thermal runaway tests of AFLMB pouch cells are performed with ARC. We study the effects of state of charge (SOC), cycling number, and electrolyte recipes on AFLMB battery safety. By analyzing the onset temperature of DSC and temperature rate (dT/dt) of ARC, it can be found that different solid electrolyte interphases (SEIs) derived from different electrolytes can affect the thermal stability of deposited Li, resulting in different thermal runaway paths and maximum temperatures. Through the ARC-DSC combined diagnosis, we find that local high concentration electrolyte (LiFSI:DME:TTE = 1:1.2:3 by mol, denoted as LHCE) improves the thermal stability of the battery via the passivation of deposited Li by SEI. Furthermore, the morphology and surface composition of the anode before and after cycling is studied via scanning electron microscopy (SEM) and X-ray photoelectron spectroscopy (XPS). It reveals that the SEI derived from LHCE can passivate Li metal and generate a more uniform lithium deposition. While the deposited lithium in the 1M $LiPF_6$ in EC/DEC (1/1, v/v) (denoted as LP40) electrolyte was much more dendritic, especially after cycling at high current densities, leading to a change in reactivity of lithium. Consequently, in safety tests of different battery systems, the ARC-DSC combined diagnosis explains the safety difference between lithium ion and anode free batteries.

2. Results and discussions

2.1. Comparison of battery safety test methods

There are many types of thermal analysis experiments for assessing battery safety. NP, ARC, and DSC are intensively applied in both industry and academia. NP and ARC are mostly used for large-scale pouch cells, while the DSC is used to study the thermal stability of single/multiple components in batteries. These battery safety data are usually collected independently, without cross-comparison, due to the knowledge gap of the scale effect. As shown in Fig. 1a, nail penetration experiments are applied to simulate an internal short circuit by inserting a nail into the pouch cell, which will lead to a rapid temperature rise and potentially thermal runaway. The temperature sensor is usually embedded in the tip of the nail, providing localized heat generation during penetration. Although it is widely used as a crucial test in the battery industry, the repeatability of this test is poor [12]. Even with automated equipment, the detected peak temperature will vary greatly based on the nail penetration position, needle angle (vertical or inclined), and penetration speed.

ARC tests measure the thermal stability and thermal runaway (TR) characteristics of a pouch cell with heat-wait-search (HWS) mode under adiabatic conditions. It can determine the onset and peak temperature of thermal runaway and analyze self-heating rates. The HWS system compares the heating rate to find whether there is an exothermic reaction. If not, it actively heats a temperature gradient until the exothermic reaction is detected [13]. As shown in Fig. 1b, the onset temperature (T_1, the point first exit the HWS mode), the critical point of self-heating (T_2, when $dT/dt = 10\ ^\circ C\ min^{-1}$), and the highest temperature of thermal runaway (T_3 or T_{max}) can be determined, which defined three stages for thermal runaway process [7,23–26]. The data of ARC can be plotted as both temperature dependence on time and self-heating rate dependance on temperature. From the plot of tempereature rate vs temperature, we can clearly define three stages. In stage I, the instrument is in HWS mode, and self-heating has not occurred. In stage II, thermal-induced side reactions cause self-heating, and heat accumulates gradually. In stage III, the thermal runaway process is caused by direct reaction of the cathode and anode or short-circuiting of the cell that releases a large amount of joule heat [27,28]. Since ARC measures self-heating rates under adiabatic conditions, it primarily detects exothermic reactions that drive thermal runaway.

The DSC test (Fig. 1c) is used to characterize the thermodynamic properties of a substance by measuring the heat flow between the sample and the reference. Since there is no heat transfer between the sample and reference, DSC is of relatively high accuracy and repeatability in quantitative calculations. Compared with ARC, DSC uses continuous external heating to detect thermodynamic behavior in the crucible, which is a kind of steady-state thermal analysis technique. The data from DSC can reflect the onset temperature of exothermic/endothermic reaction (T_{onset}), the peak temperature of heat flow (T_p), the reaction ending temperature (T_e), and the enthalpy change represented by the peak area (ΔH). Since this information is from typical thermodynamic tests, they are more reliable in characterizing the exothermic reaction or endothermic reaction process of the electrode. However, DSC is more concerned with chemical reactions instead of electrochemical reactions and is limited by a small test scale, making it difficult to characterize the safety of large batteries. For instance, with batteries assembled of the same material, the effects of different stacking processes and cell forms on thermal runaway are difficult to distinguish by DSC [3].

Comparing these methods, the NP simulates internal short circuits with direct mechanical abuse, providing realistic failure data quickly (seconds to minutes). However, it lacks a controlled thermal environment and is destructive. ARC offers precise thermal runaway analysis under adiabatic conditions, capturing self-heating rates and onset temperatures, yet it is slow (hours to days) and limited to thermal triggers. DSC excels in material-level thermal analysis (e.g., electrolyte decomposition) with fast, high-resolution heat-flow data, but its small sample size and non-adiabatic conditions underestimate full-cell risks. Fig. 1d and Tables S1–S3 summarize the key parameters of three techniques in characterizing thermal runaway of lithium-ion batteries, lithium metal batteries and anode-free lithium batteries. For the nail penetration experiment, the index of the maximum temperature of the NCM/Gr battery shows a large temperature range (400–1000 °C), similar to T_{max} obtained in the ARC test, indicating that the repeatability of these two experiments is poor. Besides, the average value of the T_{max} from nail

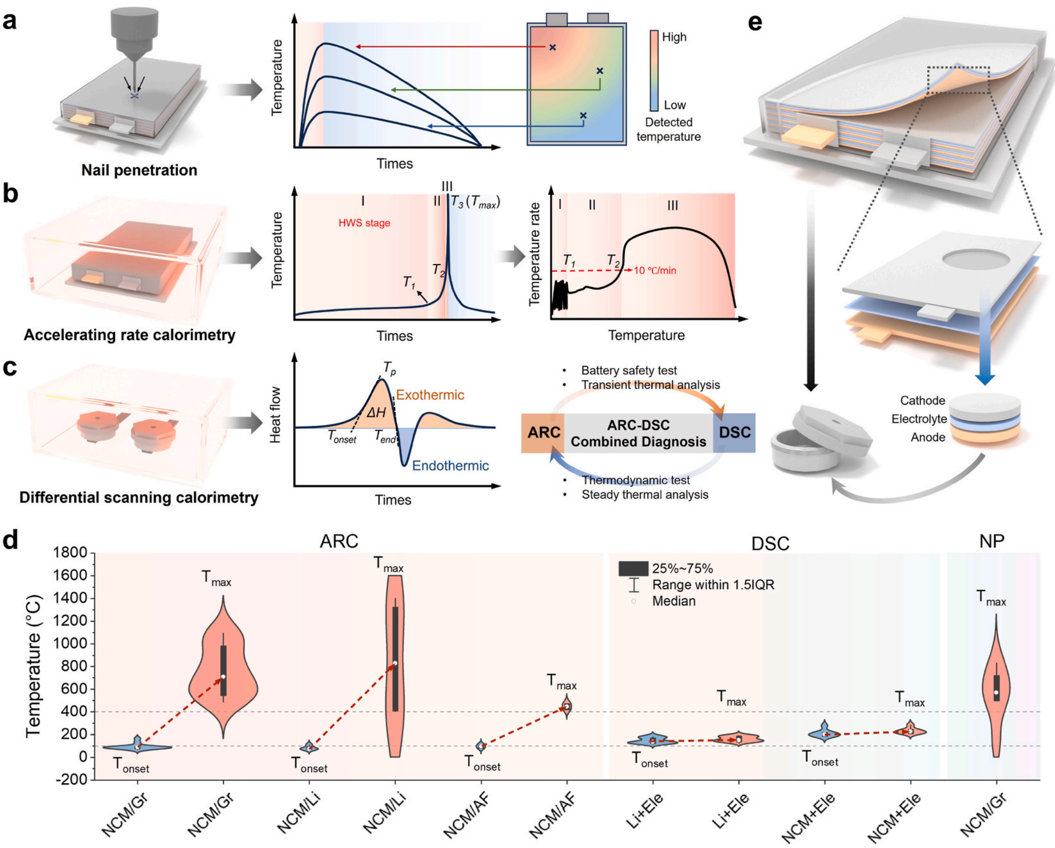

Fig. 1. Schematics of three different thermal analysis measurements, including nail penetration, ARC, and DSC. (a) Nail penetration setup for data collection. The temperature signal is significantly affected by the location, depth, and rate of the probe. (b) ARC setup and the battery safety information that can be extracted from ARC test curves. (c) DSC setup and the thermodynamic information that can be extracted from DSC test curves. (d) Comparison of safety parameters of different lithium batteries using ARC, DSC and nail penetration. Data using pouch cells data that come from Tables S1–S3. In the ARC section, a comparison was made between lithium-ion batteries (NCM/graphite), lithium metal batteries (NCM/Li), and Anode-free batteries (NCM/AF). In the DSC section, the parameters of the first exothermic peak among different components, for example anode plus electrolyte (Li + Ele) and cathode plus electrolyte (NCM + Ele), were summarized. (e) Scale effect of battery safety test. The pouch cells are usually used in the nail penetration and ARC test. The coin cells are used in the DSC test.

penetration is lower than the that of ARC, since the nail penetration test is not in a adiabatic condition and characterizes local short-circuit heat release, while ARC represents thermal runaway heat release throughout the entire battery package. Therefore, ARC is relatively more accurate than nail penetration. Notably, anode free cells show higher T_{onset} and lower T_{max} than the NCM/Gr cells and NCM/Li cells. For the DSC test, the onset temperature of reaction between Li metal and electrolyte is lower and closer to the T_{onset} of ARC measurement. This demonstrates that metallic lithium may be an important factor influencing the onset and maximum temperature of thermal runaway, but the specific causes and pathways of thermal runaway are difficult to analyze by one single testing technique.

Both ARC and DSC can be operated on either materials or cells. However, ARC only uses external heat source when in HWS mode. The subsequent reactions are driven only by the heat released from onset reactions, making it ideal for evaluating the intrinsic thermal stability and abuse tolerance of energy storage devices. In contrast, DSC continuously heats the sample with an external source and activates reactions once a sufficient temperature is reached, so it is better suited for identifying and quantifying battery side reactions. To better understand battery safety of AFLMBs, the configuration parameters of the pouch cell can be simulated into the coin cell to achieve exothermic diagnosis, due to the uniformity of materials and structures (Fig. 1e). However, the scale effect within pouch cells and button cells can cause a huge difference in thermal failure. For example, in pouch cells, the electrode area and stacking pressure (0.2–1.4 MPa) of the electrode sheets are higher than those of coin cells (10–100 kPa) [29,30]. Quantity of electrolyte in coin cells is difficult to control due to the large dead volume, while the electrolyte/capacity (E/C) ratio of pouch cells is controlled to be 3 g/Ah. This means that the heat required to raise the temperature of a coin cell by one degree will be higher than that of a pouch cell. Furthermore, the limitations of thermal analysis techniques expand the scale effect. For example, ARC can not pinpoint the local reaction of thermal runaway, like Li reaction with electrolyte and SEI decomposition. While DSC can only monitor chemical processes instead of electrochemical processes. Understanding these differences is particularly important for optimizing battery safety evaluation.

2.2. The SOC effects in thermal runaway

Since the thermal stability of a battery depends strongly on its SOC [31], the SOC effect on battery safety of NCM811/Cu AFLMBs using LP40 electrolyte was first investigated by using different measurement techniques. The 2Ah pouch cells were assembled for ARC tests. Fig. 2a–c shows the temperature, voltage, and temperature rate profiles of the NCM811/Cu pouch cells at 0, 50 %, and 100 % SOC for the ARC test. As shown in Fig. 2a–c, the onset temperature of the 100 %-SOC cell is about 61.5 °C (T_1), where self-heating begins to accumulate heat. When the cell temperature reached about 162.5 °C (T_2), the temperature rate increased to 10 °C min^{-1}, indicating that the heat generated by self-heating has accumulated to a certain extent and triggered thermal runaway. The thermal runaway temperature rate started to rise more quickly. And it reaches its maximum temperature (T_3) at 437.9 °C. The cell voltage began to decrease instantly to almost 0V (Fig. 2b), and an

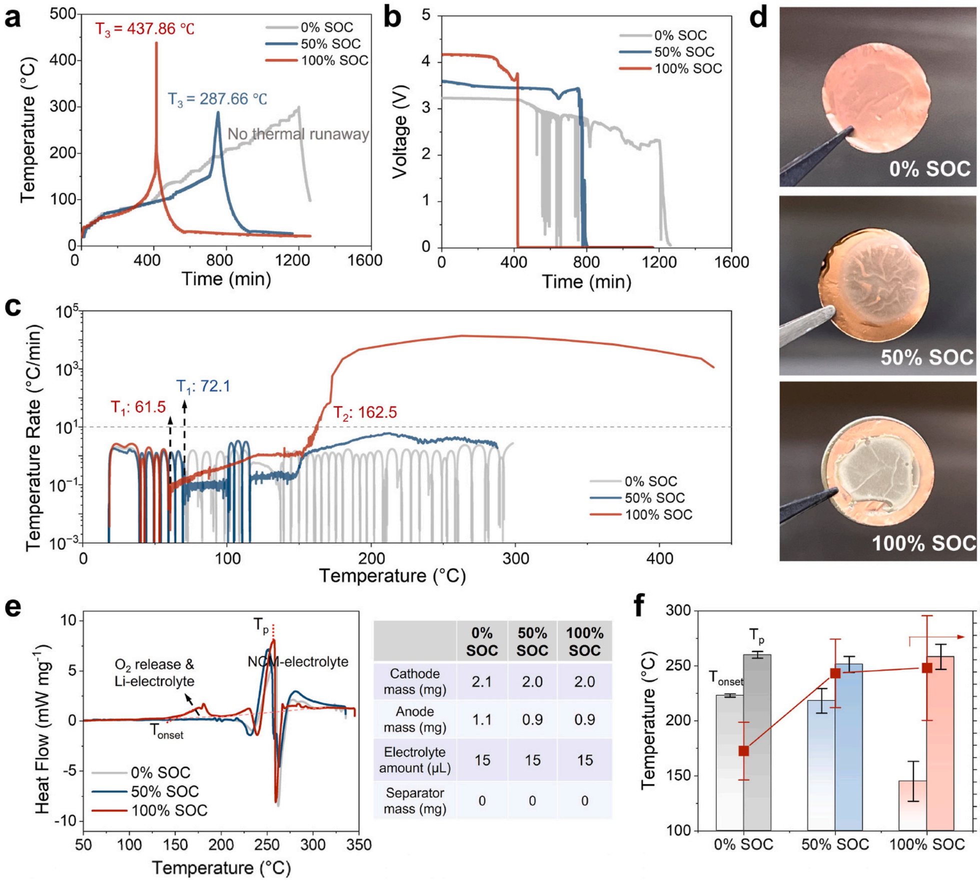

	0% SOC	50% SOC	100% SOC
Cathode mass (mg)	2.1	2.0	2.0
Anode mass (mg)	1.1	0.9	0.9
Electrolyte amount (μL)	15	15	15
Separator mass (mg)	0	0	0

Fig. 2. State of charge effect on the safety of anode-free Li metal batteries. (a) The temperature profile with test time of the ARC test of the NCM811/Cu pouch cell (2 Ah) at different SOCs with 1M $LiPF_6$ EC-DEC (1/1, v/v), i.e. LP40 electrolyte. (b) Voltage profile with test time and (c) temperature rate profile. (d) Digital photos of the disassembled anode from NCM811/Cu anode free battery under 0 % SOC, 50 % SOC, and 100 % SOC. (e) DSC profiles of NCM811/Cu micro-coin cell under different SOCs without a separator in LP40 electrolyte. The table shows the corresponding setup parameters. The capacity loading of NMC811 is 0.674 mAh/g. (f) Related thermodynamic parameters and total enthalpy change of the NCM811/Cu micro-coin cell from DSC.

obvious thermal runaway occurred, reaching a temperature rise rate of about 13700 °C min^{-1}. For the cell of 50 % SOC, as shown in Fig. 2c, it exited HWS-mode after 115 min at about 72.1 °C for the first time, and after about 350 min of self-heating, it returned to HWS mode again. When the cell was heated to 120 °C, it exited HWS-mode the second time and constantly heated itself, until finally reaching the maximum temperature of 288 °C, at which time short-circuiting occurred, and the voltage dropped to almost 0 V. Fig. S1 summarized the T_3 and maximum dT/dt changes with increasing SOC. Notably, the dT/dt of 50 % SOC and 0 % SOC cells were much lower (less than 10 °C min^{-1}) than that of 100 % cell, which means they experience very little or even no thermal runaway. Therefore, in AFLMB cells, higher SOC is going to cause higher T_3 and self-heating rate.

As a complement, the NCM811/Cu micro-coin cells in different SOCs were characterized by DSC. After the coin cell was charged to the specified SOC, it was disassembled to obtain a cycled cathode and anode (Fig. 2d), and then further assembled into a micro-coin cell without a separator in a DSC crucible. Notably, as shown in Fig. 2e, the 100 % SOC cell exhibits an exothermic peak at around 160 °C. It can be assigned to the oxygen release and NCM811 decomposition [32,33]. However, no significant exothermic peaks were observed in the 50 % SOC cell and 0 % SOC cell, which was consistent with the ARC results. Besides, the endothermic peaks at 240 °C and 260 °C, and the exothermal peak at around 250 °C are attributed to the reaction between the cathode material and the electrolyte (Fig. S2). From the corresponding parameters from Fig. 2f, the onset temperature of the 100 % SOC cell is significantly lower than that of the 50 % SOC and 0 % SOC cells, which means that the 100 % SOC battery has a more violent exothermic reaction. In addition, the total enthalpy change of the 100 % SOC cell is 0.33 J mg^{-1} higher than the 50 % SOC (0.32 J mg^{-1}) and 0 % SOC cells (0.16 J mg^{-1}). When considering the separator, as shown in Fig. S3, the exothermic peak of oxygen release is suppressed, accompanied by a higher enthalpy change (0.63 J mg^{-1} for 100 % SOC) that varies with SOCs. This is because the separator acts as a physical barrier between the cathode and the anode, which in turn alters both heat and mass transfer. The separator layer adds additional thermal resistance and contributes to thermal spreading, slowing the local temperature rise and weakening the positive feedback between oxygen evolution and exothermic reactions. Compared with the ARC and DSC (Table S3), the detection results of DSC and ARC on the thermal runaway reaction caused by the SOC effect are consistent. The heat release in the battery showed a positive correlation with the increase in SOC. Both ARC and DSC results confirmed the dependence of the thermal stability of cells on SOCs and that cells with higher SOCs have lower onset temperature and much higher temperature rate during thermal runaway, meaning that fully charged cells have much more severe safety concerns [34].

2.3. Electrolyte and cycle number effects on battery safety

We further measured the changes in the thermal properties of AFLMBs with different cycle numbers and electrolytes by using ARC and DSC techniques. The thermal stability of NCM811/Cu pouch cell fully charged at C/10 using LP40 electrolyte after 1 cycle and 20 cycles were compared. For both electrolytes, a higher cycle number is going to increase the T_3 of thermal runaway, which is consistent with Li ion batteries. As shown in the DSC profiles (Fig. 3a), the 1-cycle cell of LP40 shows a significant peak at around 180 °C, which can be derived from the direct reaction of melted lithium metal with electrolyte (Li-electrolyte) [35]. After that, a shoulder peak at around 240 °C indicates the electrolyte decomposition. While the LHCE cell exhibits an endothermic peak that can be assigned to Li melting at 180 °C, and begins to react with the electrolyte at around 228 °C. In Fig. S4a, we performed the DSC test of pure LP40 electrolyte. Compared to the data in Fig. 3a and b, the peaks at around 260 °C and 335 °C can be assigned to electrolyte decomposition [36]. For the 20-cycle cell in Fig. 3b, the Li-electrolyte reaction of LP40 occurs earlier at around 140 °C. And peaks at around 238.5 °C and 262.5 °C are derived from the decomposition reaction of the electrolyte. Compared with the thermal properties of the cell with LP40 electrolyte, the cell with LHCE exhibits lower enthalpy changes and a postponed starting point of exothermic reaction. Notably, the reaction of Li and electrolyte occurred after Li melting in all LHCE cells. This is because the SEI formed by LHCE is denser and inorganic-rich. Even if there is a slight SEI breakdown and regeneration before Li melts, the net reaction rate of the lithium electrolyte and the related heat release remain relatively low and cannot contribute to a peak in the DSC curve. After Li melts, the interfacial wettability is enhanced, the specific surface area and the mass transfer rate increase, inducing a more severe Li-electrolyte reaction. However, LP40 tends to form a less dense, more organic/porous SEI that is less protective, so significant Li electrolyte reaction can already occur when Li is still solid, leading to earlier onset and faster growth of self-heating, which indicating the properties of the SEI play a crucial role in controlling the reactivity of Li with the electrolyte.

Fig. 3c–d shows the temperature and temperature rate profiles of the 1-cycle cells. The LHCE cell reached its maximum temperature (T_3: 494.8 °C) after ~700 min, while the cell with LP40 electrolyte reached T_3 (437.9 °C) at ~410 min. From the temperature rate changes (Fig. 3d), the T_1 and T_2 of the 1-cycle LP40 cell are about 63.9 °C and 162.5 °C, while for the LHCE cell, they are 53.3 °C and 176.9 °C, indicating that although the onset temperature of LHCE is lower, the intensity of its thermal runaway process is less than that of LP40. This can also be reflected in the temperature rate. The maximum temperature rate of LHCE

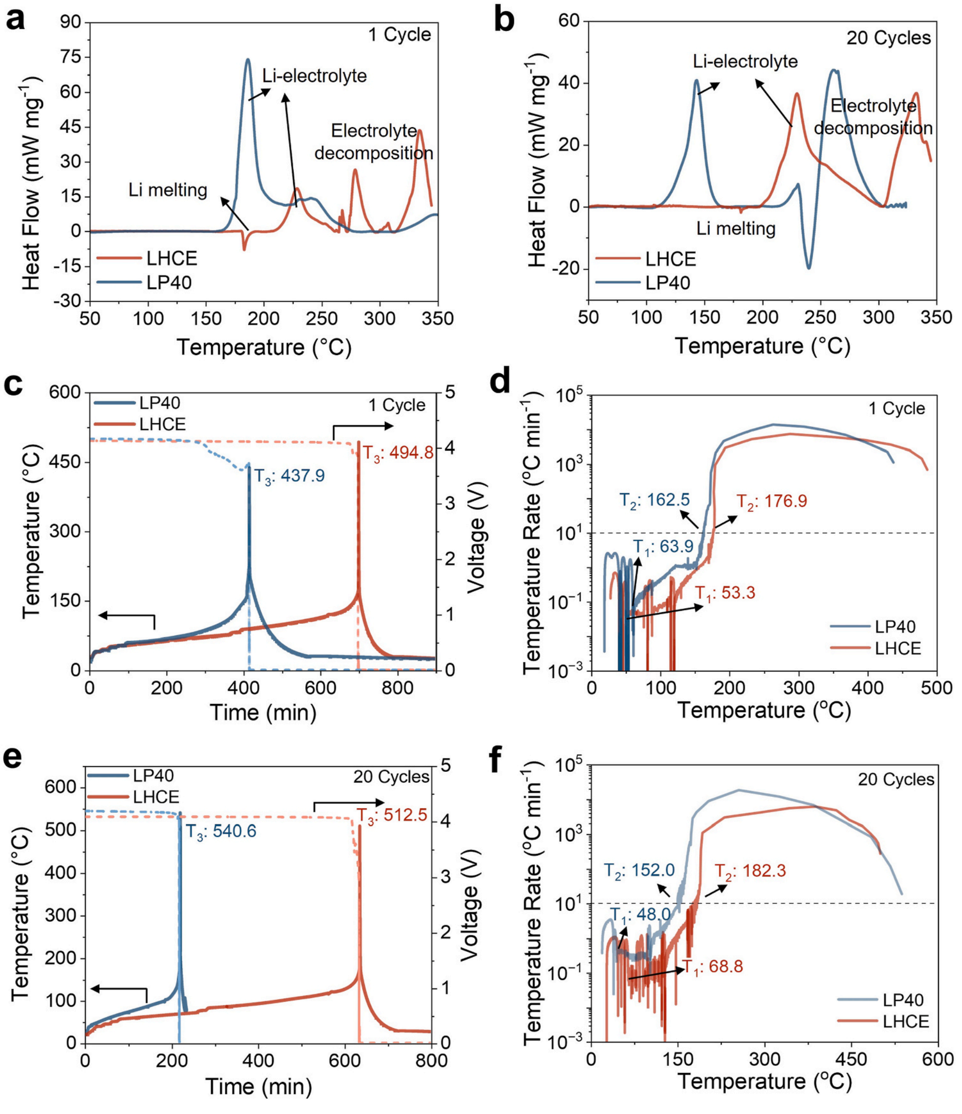

Fig. 3. Electrolyte and cycle number effect on the safety of cycled Li metal anode and anode-free Li metal pouch cells (2Ah). (a) DSC profiles of LP40 and LHCE electrolyte with Li deposited Cu foil under C/10 rate after 1 cycle. (b) DSC profiles of LP40 and LHCE electrolyte with Li deposited Cu foil under C/10 rate after 20 cycles. (c) The temperature and voltage profile of the ARC test of the NCM811/Cu full cell after 1 cycle with LP40 and LHCE electrolyte under C/10 rate. (d) Corresponding temperature rate profile with temperature for 1 cycle cells. (e) The temperature and voltage profile of the ARC test of the NCM811/Cu cell after 20 cycles with LP40 and LHCE electrolyte under C/10 rate. (f) Corresponding temperature rate profile with temperature for 20 cycles cells. All the ARC and DSC tests are performed under 100 % SOC and C/10 charging rate.

(7361 °C $\min^{-1}$) is significantly lower than that of LP40 (13701 °C $\min^{-1}$). For the 20-cycle cells in Fig. 3e, the maximum temperature of the LP40 cell was 540 °C at 220 min, while the LHCE cell did not reach a maximum temperature of 512.5 °C until 740 min. Under condition of 20 cycles in Fig. 3f, the LP40 cell shows lower T_1 (48 °C) and T_2 (152 °C) than that of LHCE (T_1: 68.8 °C, T_2: 182.3 °C), but higher maximum temperature rate of 18434 °C $\min^{-1}$ than that of LHCE (6143 °C $\min^{-1}$). Fig. S5 compares the variation degree of key parameters of thermal runaway caused by aging in different electrolytes. It can be seen that the changes of LHCE batteries at the highest temperature T_3 and the highest temperature rate dT/dt after long cycles are significantly weaker than those of LP40 batteries. These results indicate that LHCE can effectively passivate Li and mitigate the severity of thermal runaway.

For a better understanding of battery safety between coin and pouch cells, we plotted DSC and ARC data with the same temperature scale. In ARC test data analysis, the T_1 value is usually treated as the temperature where self-heating begins (e.g., SEI decomposition). However, the $T_{Li\text{-}elect}$ caused by thermal decomposition of SEI in DSC is much higher than the derived T_1, close to that of T_2. As shown in Fig. 4a, for the 20-cycled cell with LP40 electrolyte, the change in heat flow begins to increase as early as 50 °C. At this point, it is when the self-heating stage begins for the first time in the ARC. The SEI formed by the LP40 electrolyte after cycling has poor thermal stability, since the heat released by self-heating will cause the continuous decomposition of the SEI, thereby leading to a continuous increase in the heat flow in the DSC. While this situation does not happen for the 1-cycle cell due to insufficient SEI. Notably, for the 1-cycle cell, the temperature at which lithium begins to react directly with the electrolyte in DSC corresponds to the critical temperature point (T_2) of the ARC, while the same reaction occurs in advance in 20-cycle cells. These differences caused by SEI are usually difficult to detect from the assessment of ARC. In Fig. 4b, it can be seen from the DSC curve of the LHCE cell that during the early heating process, the 20-cycle cell experienced a small temperature fluctuation, since the SEI formed by the LHCE can stabilize heat release to a certain extent.

Considering these results of ARC and DSC and the existing literature, [13,23,37,38] the thermal runaway process of cells with LP40 and LHCE after cycling can be depicted as Fig. 4c-d. When the battery starts the self-heating stage, the heat generated by self-discharge drives the decomposition of the SEI. In the LP40 cells, the decomposition product of $LiPF_6$ (PF_5) undergoes reactions with Li_2O and Li_2CO_3 in the SEI to form inorganic components [23]. The decomposition of the SEI further leads to the reaction between the electrolyte and dendrite lithium, generating a large amount of heat. Subsequently, the battery enters a rapid internal short circuit stage, intensifying thermal runaway and inducing decomposition of the cathode and electrolyte as well as oxidation reactions of residual organic products. For the LHCE cells (Fig. 4d), the decomposition of SEI is not accompanied by a severe reaction between Li and electrolyte, but rather generate more inorganic components to alleviate the Li-electrolyte reaction. A large amount of heat release does not occur until Li melts. The SEI delays the premature reaction of Li with the electrolyte and further generates fluorine-containing components with high thermal stability in the subsequent process. The thermal behavior of the battery in ARC also shows the same trend, which enters the HWS mode multiple times after leaving it for the first time, indicating that the SEI passivates heat transfer during the self-heating stage of the battery. This is the reason the LHCE cells show higher thermal stability than the LP40 cells.

2.4. Impact of charging rate on anode morphology and DSC results

For anode free batteries, lithium sources all came from the cathode, whose deposition morphology and reactivity on the copper collector determined the thermal runaway self-heating route [3]. Besides, the decay of the cell mainly originated from degradation at the anode, which

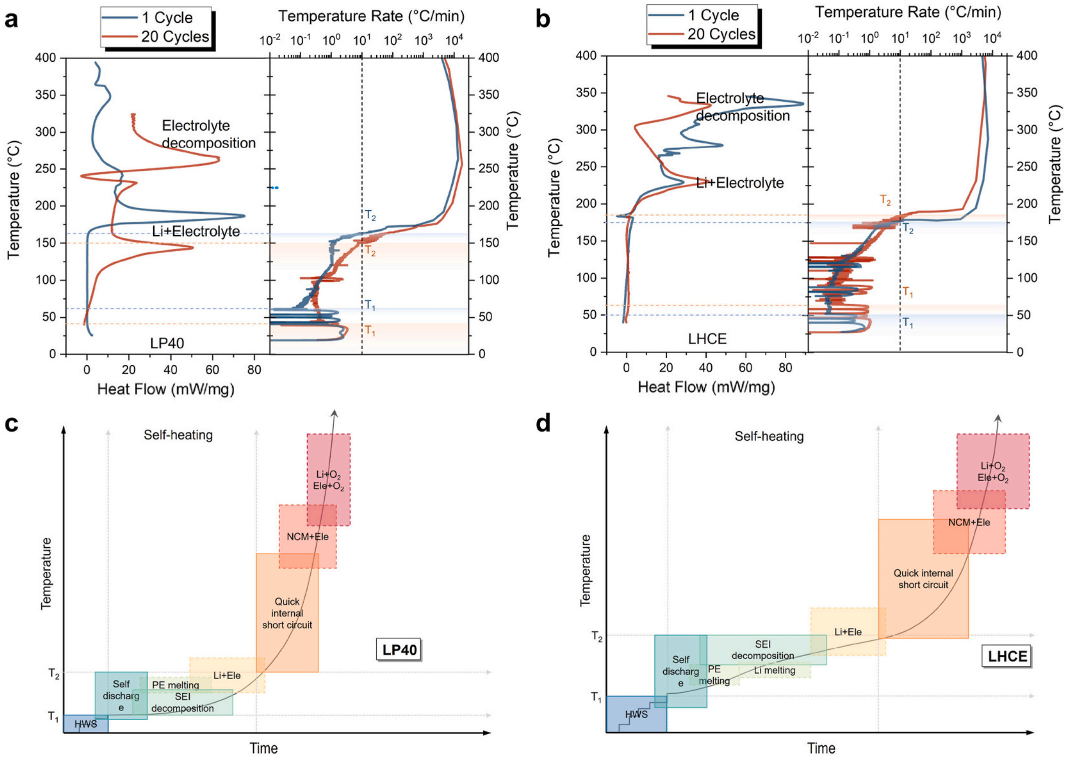

Fig. 4. Difference between ARC and DSC in revealing cycling effects and thermal runaway pathway of different electrolytes. (a) Temperature profile comparison of DSC measured by using LP40 electrolyte with deposited Li on Cu foil after 1 cycle and 20 cycles under C/10 rate, and ARC measured by using anode-free Li metal pouch cells (2Ah) after 1 cycle and 20 cycles under C/10 rate. (b) Temperature profile comparison of DSC and ARC by using the same configurations of the cell with LHCE electrolyte. (c) Schematic illustrations of the main process during thermal runaway for 20-cycle cells with LP40 electrolyte and (d) LHCE electrolyte.

determined the battery safety. Therefore, the thermal properties of deposited Li under different rates after 20 cycles in LP40 electrolyte were measured by DSC as shown in Fig. 5a. The impact of increasing the charging rate indicates that the starting points of all reactions are advanced, which is consistent with the 1-cycle cells (Fig. S6a) [35]. The initial columbic efficiencies and discharge capacity of these cells decayed rapidly in the first 20 cycles at different rates (Figure S7a and Figure S8). Compared with the capacity loss of cells under C/3 (Table S5), the AFLMB with LP40 electrolyte undergoes more capacity loss as the increase of current density. The inefficiency in plating and stripping caused the continuous formation of highly dendritic and reactive lithium, which may lead to a higher self-heating rate. Fig. 5b–c shows the morphology of the deposited lithium anode in LP40 electrolyte after cycling under a current density of C/3 and C/10. The SEM grayscale standard deviation (StdDev) was further adopted to characterize the surface roughness index of the electrode.Compared with the 1-cycle cell (Fig. S9), after 20 cycles, the anode under both C/3 and C/10 became a lot more dendritic. Moreover, with the increase of current density, the StdDev value increases, which means the deposition morphology of the anode became more and more disordered and more lithium dendrites formed. In terms of deposition thickness (Fig. 5d), for the LP40 electrolyte, lower current density tends to form a denser and thicker lithium metal layer, while high current density shows a mixed-phase dendritic-based deposition layer, which is consistent with the capacity loss trend. This is because the formation of dendrites can block the continued deposition of reversible lithium metal under high current density.

In comparison, as shown in Fig. 5e and Fig. S6b, the current density has a more significant impact on the safety of the battery with LHCE. With the decrease of the current density, the total enthalpy change in LHCE cells decreases significantly. In addition, no exothermic reaction between lithium and the LHCE was observed before the lithium melting peak. From the battery performance, the capacities of the LHCE cells were much steadier (Fig. S7b). The initial columbic efficiencies were 97.1 %, 96.19 % and 95.25 % for the cells cycled at C/10, C/6, and C/3, respectively. The average CE of cells was much higher (>97 %) than that of LP40 cells. Besides, LHCE shows less capacity loss than LP40 electrolyte while maintaining high capacity (Fig. S10). The thermal analysis and battery performance indicate that the LHCE electrolyte has a much higher compatibility with deposited lithium. The deposited lithium anodes in LHCE (Fig. 5f–g and Fig. S11) were further characterized. It can be found that the size of the granules increased with decreasing current density, while StdDev value decreased, indicating a more uniform surface. Combined with the result from the LP40 anode, the electrodeposited lithium under high current density has a smaller size and a rougher surface and tends to release more heat due to its higher reactivity (as shown in Fig. S12a). Correlate the deposition thickness and total enthalpy changes (Fig. 5d and h, Figure S12b), the deposition thickness under C/10 is thinner than that formed under higher current density in LHCE cells, which is opposite with LP40 cells. However, the deposition thickness is positively correlated with the total enthalpy changes. This reflects that the morphological roughness and thickness of the deposited lithium surface will affect its reactivity and thermal stability with the electrolyte. Smaller size, higher roughness and thicker deposition thickness will lead to higher heat release.

In addition to the lithium deposition, the composition and uniformity of SEI have a great effect on the deposition of lithium. Both can increase concentration gradients of lithium ions, which may result in dendritic growth of lithium before the bulk electrolyte diffusion limitation and cause cell failure [39]. The XPS was used to study the elemental composition of the surface of the anodes obtained from the disassembled cells. In Fig. S13a, for a 1-cycle anode with LP40 electrolyte, the cells showed inorganic species such as LiF (at about 684.2 eV) and $Li_xPO_yF_z$ (at about 686.2 eV), which may be due to decomposition of $LiPF_6$. In C 1s spectra of Fig. S13b, peaks of C-C (285.0 eV), C-O (286.6 eV), O-C=O (at about 288.8 eV), and poly(O-C=O) (at about 290.8 eV) can be observed due to the decomposition of the carbonate solvents. After 20 cycles as shown in Fig. 5i, $LiPF_6$ (at about 688.4 eV from the F 1s peaks) was detected. The binding energy of the $Li_xPO_yF_z$ peak was decreased by 0.7 eV (685.5 eV) compared with 1-cycle anode. Besides, the binding

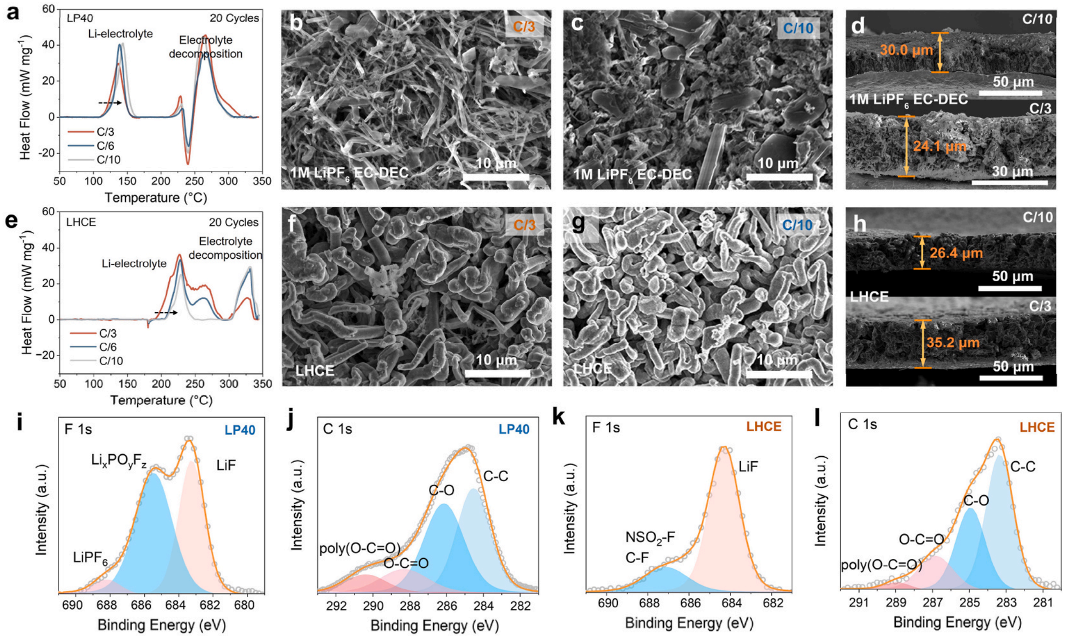

Fig. 5. Charging rate effect on battery safety of anode free Li metal batteries. (a) The DSC profile of NCM811/Cu coin cells with LP40 electrolyte after 20 cycles under different charging rates. (b) SEM images of the anode from the NCM811/Cu coin cells with LP40 electrolyte after 20 cycles under C/3 rate, and (c) under C/10 rate. (d) Corresponding SEM image of cross cross-section for the anode Cu collector. (e) The DSC profile of NCM811/Cu coin cells with LHCE after 20 cycles under different charging rates. (f) SEM images of the anode from the NCM811/Cu coin cells with LHCE cycled after 20 cycles under C/3 rate, and (g) under C/10 rate. (h) Corresponding SEM image of the cross-section for anode. (i) The XPS F 1s and (j) C 1s spectra of the anode after 20 cycles at the current density of C/3 with LP40 electrolyte. (k) The XPS F 1s and (l) C 1s spectra of the anode after 20 cycles at the current density of C/3 with LHCE.

energy of peaks belonging to C-O (286.2 eV) and O-C=O (288.4 eV) were decreased as well after 20 cycles in Fig. 5j. These changes in peaks indicate continuous decomposition of the electrolyte on the anode.

For the 1-cycle anodes with LHCE (Fig. S14), the SEI contains more inorganic species compared to those with LP40 electrolyte. After 20 cycles, the content ratio of LiF on the LHCE in Fig. 5k and Fig. S15 was much stronger, which is more thermally stable [40]. From the C 1s spectra in Fig. 5l, peaks of C-O and O-C=O were decreased compared with the anode using LP40 electrolyte. More lithium fluoride and anion-based inorganic compounds were generated and became relatively stable after SEI formation. This was likely due to the high concentration of LiFSI in the LHCE electrolyte, in which the solvation structure of electrolytes was effectively altered with few free solvent molecules. The anions participated in the solvation structure of Li ions and desolvated on the anode, which rendered the inorganics-rich SEI [41]. By correlating the inorganic LiF component and key parameters from ARC as shown in Fig. S16, the influence of LiF content in SEI on the thermal runaway process has been revealed. An increase in LiF percentage will raise T_1 and T_2 temperatures and reduce the maximum temperature rate, which means that LiF in the SEI to some extent alleviates the severity of thermal runaway since its stable chemical properties can reduce the catalytic reactivity at the interface. Based on the characterization of anode morphology and total enthalpy change analysis (Fig. S17), the LHCE derived SEI has better thermal stability and lithium passivity compared to the LP40 derived SEI. When the current density is C/10, LHCE tends to form a stable SEI due to relatively uniform lithium deposition. The more stable SEI passivates the reactivity of deposited lithium, resulting in a lower enthalpy change than that of LP40 cells.

2.5. Comparing safety of LIB and AFB

Furthermore, the thermal stability of the anode free cells and conventional lithium-ion cells was compared by ARC-DSC combined diagnosis. As shown in Fig. 6a, the heat flow of LP40 electrolyte lithium-ion battery with lithiated graphite (LP40-Gr LIB) was very steady and did not show a peak until the temperature reached 245 °C. Since the reactivity of lithiated graphite is lower than deposited lithium, the observed exothermic peaks were weaker than the peaks of anode-free batteries, and these peaks mainly originate from the electrolyte reaction with metallic Li. These were consistent with the data from the ARC tests in Fig. 6b, that the onset temperature of the LP40-Gr LIB was about 157.3 °C, which was far behind the AFB-LP40 (63.9 °C) and AFB-LHCE (53.3 °C). Similarly, the T_2 of the LP40-Gr LIB was about 216.6 °C, which was much higher than the AFB-LP40 (163 °C) and AFB-LHCE (181 °C) as well. Also, the highest temperature rate for the LP40-Gr LIB was significantly lower than the anode free cells, resulting in a lowest maximum temperature of 414.5 °C for LP40-Gr LIB that was 24.1 °C lower than the AFB-LP40 and 86.6 °C lower than the AFB-LHCE. From the overall DSC-ARC combined safety test, the safety of these three batteries follows the following order: LP40-Gr LIB > AFB-LHCE > AFB-LP40. Compared with LP40, LHCE does offer a relatively higher safety margin, but AFLMB can still experience dangerous thermal runaway events. This means that merely reducing Li inventory and adopting an anode free battery configuration is not sufficient to make the battery intrinsically safe.

3. Conclusions

In this work, we combined ARC tests on 2 Ah NCM811/Cu pouch cells with DSC diagnosis on matched coin cells to compare thermal analysis methods and clarify the thermal runaway mechanism of AFLMBs in LP40 and LHCE electrolytes. By aligning the temperature scales of ARC and DSC, we show that thermal runaway of AFLMBs is mainly governed by deposited Li and its SEI, and that higher SOC, higher C-rate, and longer cycling will all lower the onset temperature and increase the self-heating rate, leading to more severe thermal runaway. Comparing LP40 with LHCE reveals that the SEI derived from LHCE is more inorganic-rich and compact, which suppresses large-scale Li-electrolyte reactions until after Li melting, increases T_1/T_2, and reduces the maximum dT/dt and the sensitivity to cycling, whereas LP40 forms a more porous SEI that allows earlier Li-electrolyte reactions, more dendritic Li, and higher heat release. ARC-DSC combined with SEM/XPS further indicates that higher LiF content and smoother Li morphology improve thermal stability, while rough, dendritic and thicker Li deposits are associated with stronger exothermic behavior. Under otherwise similar conditions, conventional LP40-Gr lithium-ion cells show higher onset temperatures, lower dT/dt, and lower Tmax than AFLMBs, which means their safety is still better. Overall, our results suggest that the current safety level of NCM811-based AFLMBs is not satisfactory; simply reducing lithium inventory is not sufficient, and further safety improvement will require careful engineering of SEI and controlling of deposited-Li morphology.

4. Experimental details

4.1. Electrolyte and electrode preparation

The 1M $LiPF_6$ in EC/DEC (1/1, v/v) electrolyte (1 mol $LiPF_6$ in EC:DEC = 1:1 (volume ratio)) and the localized high-concentration electrolyte (LHCE, LiFSI:DME:TTE = 1:1.2:3 in molar ratio) were prepared in an argon gas filled glove box with O_2 and $H_2O < 0.1$ ppm. Commercial $LiNi_{0.8}Co_{0.1}Mn_{0.1}O_2$ (NCM811, 3.8 mAh cm^{-2}, with 2 wt% PVDF and 2 wt% Super P) electrode was obtained from Amperex Technology Limited

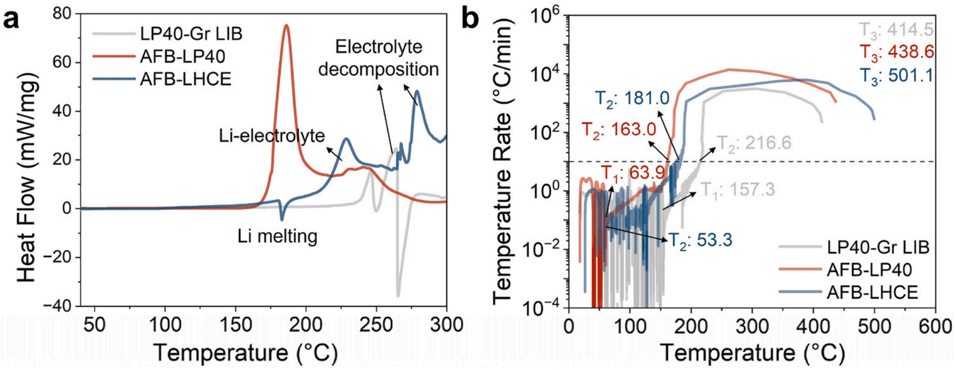

Fig. 6. Comparison of battery safety for lithium-ion battery and AFLMB. (a) DSC profile of lithiated graphite or deposited lithium with electrolytes (electrode materials were cycled under C/3 for 1 cycle, 100 % SOC, capacity: about 2 mAh); (b) ARC tests of a lithium-ion battery, anode-free battery using LP40 electrolyte (Pouch cells (2 Ah) were cycled under C/3 for 1 cycle, 100 % SOC).

(ATL) in China. The electrode was punched into disks with a diameter of 12 mm and dried in a vacuum at 80 °C for 24 h before use.

4.2. Coin cell and pouch cell assembly

CR2032 coin cells were assembled by using NCM811 disk as the cathode, polyethylene (Celgard 2035) as the separator, copper foil (25 μm, 15 mm in diameter) as the anode, and 30 μL of LHCE or 1M $LiPF_6$ in EC/DEC (1/1, v/v) electrolyte was added. To avoid corrosive reactions between solvents and coin cell parts for the LHCE electrolyte, alumina-clad-coated coin cell cases were used. The assembled cells were rested at OCV overnight before any electrochemical measurements were performed.

Anode-free pouch cells were assembled in a dry room. The double-side-coated anodes and cathodes were cut into 74mm × 46 mm and 72mm × 45 mm sheets (with an extended current-collector tab). The cathode and anode sheets were then alternatively hand-stacked with separator between any two sheets. Then the anode and cathode current-collector tabs were wielded with a Ni and Al tab, respectively, by an ultrasonic wielding machine, respectively. The electrode stack was fitted in a pouch and then sealed on three sides, and then dried at 80 °C in a vacuum for 24 h. After drying, electrolyte was injected into the pouch cell (3 g/Ah) followed by vacuum-sealing.

4.3. Electrochemical measurement

All cells were first charged and discharged at a current density of C/20 (0.19 mA cm^{-2}) for activating batteries using the 3200A LAND battery test system. For 100 % SOC, first using constant current charging the battery to 4.2 V at a current density of C/6, then further charging the battery by using constant voltage (4.2 V) mode until the current density is smaller than C/20 for depolarization. The charge-discharge profiles of the cell were measured in the voltage range of 2.8–4.2 V at specific current densities (C/3, C/6, and C/10).

4.4. Ex-situ calorimetry

Ex-situ experiments were performed with a SETLINE differential scanning calorimeter. High-pressure (100 bar) stainless steel crucibles were used, with a gold seal to prevent explosion. The sample capsule contains fresh electrolyte (about 15 μl) and deposited lithium (about 3 mg) from the charged or cycled cell, and the reference capsule has no samples. Differential scanning calorimetry was conducted by heating the sample and reference capsules from 40 °C to 350 °C at a ramping rate of 5 °C min^{-1}. After the test, the crucibles were opened and thoroughly cleaned before reused. For the 0 %, 50 %, and 100 % SOC cells, the DSC measurements were repeated twice for each condition and averaged.

4.5. Accelerating rate calorimetry (ARC) test

ARC was conducted with an accelerating rate calorimeter by thermal hazard technology. A cell was placed inside a chamber, and the real-time OCV and temperature of the cell were measured. The ARC tests were conducted in a heat-wait-seek (HWS) procedure. The data was collected at a frequency of 10 Hz. After the test, the debris of the cell was removed from the chamber and collected. Before entering self-heating mode, the data was very noisy and was de-noised through binomial fitting for every 600 points (equal to 1 min). The temperature rate was obtained solely by taking the time derivative of temperature. ARC tests were performed once per cell due to the destructive and time-consuming nature of the measurements.

4.6. Electrode characterization

The morphology of the samples was investigated with the field-emission scanning electron microscopy (Apreo 2 SEM, ThermoFisher). The XPS tests were conducted on a PHI VersaProbe II scanning XPS microprobe. The samples were loaded in a glovebox and transferred into the instrument through a vacuum transfer vessel. A survey scan was first carried out, and then high resolution-scans for the elements. The CasaXPS software was used to process XPS data. First, we calibrated binding energy using the C1s peak from C-C at 284.8 eV. Then, we fitted the core peaks with a Shirley-type background and optimized the peak position/areas using 70 % Gaussian-30 % Lorentzian Voigt peak shapes and fullwidth at half-maximum (FWHM) constraint ranges.

CRediT authorship contribution statement

Dongliang Chen: Writing – original draft, Visualization, Formal analysis, Conceptualization. **Jie Liao:** Writing – original draft, Methodology, Conceptualization. **Zachary J. Trdinich:** Writing – review & editing, Validation. **Chaoyang Wang:** Writing – review & editing, Conceptualization. **Feifei Shi:** Writing – review & editing, Funding acquisition, Formal analysis, Conceptualization.

Declaration of competing interest

The authors declare that they have no known competing financial interests or personal relationships that could have appeared to influence the work reported in this paper.

Acknowledgement

D.C. and F.S. acknowledge the Assistant Secretary for Energy Efficiency and Renewable Energy, Office of Vehicle Technologies of the US Department of Energy, through the US-Germany Cooperation on Energy Storage under Contract DE-AC02-05CH11357. J.L. and F.S. thank the support from the Assistant Secretary for Energy Efficiency and Renewable Energy, Office of Vehicle Technologies of the US Department of Energy through the Advanced Battery Materials Research Program. F.S. thanks the support from the National Science Foundation under Grant No. 2239690. C.Y.W. acknowledges the support of William E. Diefenderfer chair endowment.

Appendix A. Supplementary data

Supplementary data to this article can be found online at https://doi.org/10.1016/j.jpowsour.2026.239261.

Data availability

Data will be made available on request.

References

[1] S. Nanda, A. Gupta, A. Manthiram, Anode-free full cells: a pathway to high-energy density lithium-metal batteries, Adv. Energy Mater. 11 (2) (2020) 2000804.
[2] Z. Xie, Z. Wu, X. An, et al., Anode-free rechargeable lithium metal batteries: progress and prospects, Energy Storage Mater. 32 (2020) 386–401.
[3] X. Zhang, L. Huang, B. Xie, et al., Deciphering the thermal failure mechanism of anode-free lithium metal pouch batteries, Adv. Energy Mater. 13 (8) (2023) 2203648.
[4] B. Wu, C. Chen, L.H.J. Raijmakers, et al., Li-growth and SEI engineering for anode-free Li-metal rechargeable batteries: a review of current advances, Energy Storage Mater. 57 (2023) 508–539.
[5] N. Zhang, W. Mei, Y. Li, et al., Investigation on mechanical bending caused thermal runaway of lithium-ion cell, J. Energy Storage 68 (2023) 107688.
[6] D.H. Doughty, P.C. Butler, R.G. Jungst, E.P. Roth, Lithium battery thermal models, J. Power Sources 110 (2002) 357–363.
[7] X. Feng, D. Ren, X. He, M. Ouyang, Mitigating thermal runaway of lithium-ion batteries, Joule 4 (4) (2020) 743–770.
[8] Y. Son, H. Cha, T. Lee, et al., Analysis of differences in electrochemical performance between coin and pouch cells for lithium-ion battery applications, Energy Environ. Mater. 7 (3) (2023) e12615.
[9] S. Ma, M. Jiang, P. Tao, et al., Temperature effect and thermal impact in lithium-ion batteries: a review, Prog. Nat. Sci. Mater. Int. 28 (6) (2018) 653–666.

[10] R. Kantharaj, A.M. Marconnet, Heat generation and thermal transport in lithium-ion batteries: a scale-bridging perspective, Nanoscale Microscale Thermophys. Eng. 23 (2) (2019) 128–156.

[11] D.P. Finegan, B. Tjaden, T. Heenan, et al., Tracking internal temperature and structural dynamics during nail penetration of lithium-ion cells, J. Electrochem. Soc. 164 (13) (2017) A3285–A3291.

[12] J. Xu, W. Mei, C. Zhao, et al., Study on thermal runaway mechanism of 1000 mAh lithium ion pouch cell during nail penetration, J. Therm. Anal. Calorim. 144 (2) (2020) 273–284.

[13] X. Feng, M. Fang, X. He, et al., Thermal runaway features of large format prismatic lithium ion battery using extended volume accelerating rate calorimetry, J. Power Sources 255 (2014) 294–301.

[14] B. Lu, D. Cheng, B. Sreenarayanan, et al., Key parameters in determining the reactivity of lithium metal battery, ACS Energy Lett. 8 (7) (2023) 3230–3238.

[15] L. Gan, R. Chen, X. Xu, et al., Comparative study of thermal stability of lithium metal anode in carbonate and ether based electrolytes, J. Power Sources 551 (2022) 232182.

[16] L. Liu, X. Feng, M. Zhang, et al., Comparative study on substitute triggering approaches for internal short circuit in lithium-ion batteries, Appl. Energy 259 (2020) 114143.

[17] S. Zhang, S. Li, X. Wang, et al., Nonflammable electrolyte with low exothermic design for safer lithium-based batteries, Nano Energy 114 (2023) 108639.

[18] C. Wu, Y. Wu, X. Yang, et al., Thermal runaway suppression of high-energy lithium-ion batteries by designing the stable interphase, J. Electrochem. Soc. 168 (9) (2021) 090563.

[19] M.P. Macdonald, S. Chandrasekaran, S. Garimella, T.F. Fuller, Thermal runaway in a prismatic lithium ion cell triggered by a short circuit, J. Energy Storage 40 (2021) 102737.

[20] J. Liao, R.S. Longchamps, B.D. McCarthy, et al., Lithium iron phosphate superbattery for mass-market electric vehicles, ACS Energy Lett. 9 (3) (2024) 771–778.

[21] D.D. MacNeil, J.R. Dahn, Test of reaction kinetics using both differential scanning and accelerating rate calorimetries as applied to the reaction of LixCoO2 in non-aqueous electrolyte, J. Phys. Chem. A 105 (2001) 4430–4439.

[22] M.N. Richard, J.R. Dahn, Accelerating rate calorimetry study on the thermal stability of lithium intercalated graphite in electrolyte. II. Modeling the results and predicting differential scanning calorimeter curves, J. Electrochem. Soc. 146 (1999) 2078–2084.

[23] X.Q. Xu, X.B. Cheng, F.N. Jiang, et al., Dendrite-accelerated thermal runaway mechanisms of lithium metal pouch batteries, SusMat 2 (4) (2022) 435–444.

[24] Q.-K. Zhang, X.-Q. Zhang, H. Yuan, J.-Q. Huang, Thermally stable and nonflammable electrolytes for lithium metal batteries: progress and perspectives, Small Sci. 1 (10) (2021) 2100058.

[25] R. Chen, A.M. Nolan, J. Lu, et al., The thermal stability of lithium solid electrolytes with metallic lithium, Joule 4 (4) (2020) 812–821.

[26] M. Fang, X. Yue, Y. Dong, et al., A temperature-dependent solvating electrolyte for wide-temperature and fast-charging lithium metal batteries, Joule 8 (1) (2024) 91–103.

[27] X. Feng, M. Ouyang, X. Liu, et al., Thermal runaway mechanism of lithium ion battery for electric vehicles: a review, Energy Storage Mater. 10 (2018) 246–267.

[28] J. Hou, L. Lu, L. Wang, et al., Thermal runaway of Lithium-ion batteries employing LiN(SO(2)F)(2)-based concentrated electrolytes, Nat. Commun. 11 (1) (2020) 5100.

[29] W. Chang, T. Xu, D. Steingart, Chemo-mechanical effects of stack pressure and temperature on anode-free lithium metal batteries, J. Electrochem. Soc. 169 (2022) 090530.

[30] K.L. Bassett, K.A. Small, D.M. Long, et al., Interfacial pressure improves calendar aging of lithium metal anodes, Frontiers in Batteries and Electrochemistry 2 (2023) 1292639.

[31] H.M. Barkholtz, Y. Preger, S. Ivanov, et al., Multi-scale thermal stability study of commercial lithium-ion batteries as a function of cathode chemistry and state-of-charge, J. Power Sources 435 (2019) 226777.

[32] A.W. Golubkov, D. Fuchs, J. Wagner, et al., Thermal-runaway experiments on consumer Li-ion batteries with metal-oxide and olivin-type cathodes, RSC Adv. 4 (2014) 3633.

[33] R. Jung, P. Strobl, F. Maglia, et al., Temperature dependence of oxygen release from LiNi0.6Mn0.2Co0.2O2 (NMC622) cathode materials for Li-Ion batteries, J. Electrochem. Soc. 165 (11) (2018) A2869–A2879.

[34] A. Kvasha, C. Gutiérrez, U. Osa, et al., A comparative study of thermal runaway of commercial lithium ion cells, Energy 159 (2018) 547–557.

[35] L. Hellweg, T. Beuse, M. Winter, M. Börner, Influence of lithium metal deposition on thermal stability: combined DSC and morphology analysis of cyclic aged lithium metal batteries, J. Electrochem. Soc. 170 (4) (2023) 040530.

[36] I.S. Buyuker, B. Pei, H. Zhou, et al., Voltage and temperature limits of advanced electrolytes for lithium-metal batteries, ACS Energy Lett. 8 (4) (2023) 1735–1743.

[37] Y. Zhang, D. Wang, C. Liang, Y. Han, Z. Li, Y. Huang, Design of double layer cathode electrode for improving the safety and stability of lithium-ion batteries, Chem. Eng. J. 495 (2024) 153344.

[38] W. Yu, K.-Y. Lin, D.T. Boyle, et al., Electrochemical formation of bis(fluorosulfonyl) imide-derived solid-electrolyte interphase at Li-metal potential, Nat. Chem. 17 (2025) 246–255.

[39] A. Maraschky, R. Akolkar, Mechanism explaining the onset time of dendritic lithium electrodeposition via considerations of the Li+Transport within the solid electrolyte interphase, J. Electrochem. Soc. 165 (14) (2018) D696–D703.

[40] X.B. Cheng, S.J. Yang, Z. Liu, et al., Electrochemically and thermally stable inorganics-rich solid electrolyte interphase for robust lithium metal batteries, Adv Mater 36 (1) (2024) e2307370.

[41] X. Cao, H. Jia, W. Xu, et al., Review—localized high-concentration electrolytes for lithium batteries, J. Electrochem. Soc. 168 (1) (2021) 010522.